Rare Met. (2022) 41(3):830–835
https://doi.org/10.1007/s12598-021-01836-8

RARE METALS

LETTER

Fabrication of MOF-derived mixed metal oxides with carbon residues for pseudocapacitors with long cycle life

Yuan-Fu Ren, Zhi-Liang He, Hao-Zhen Zhao, Ting Zhu*

Received: 7 June 2021 / Revised: 1 July 2021 / Accepted: 5 July 2021 / Published online: 15 September 2021

High electroactivity and good mechanical robustness of electrode materials are essential to deliver excellent electrochemical energy storage performance. Herein, metal–organic frameworks (MOF) derived mixed metal oxides (MMO, ZnO@NiO and Co_3O_4@NiO) are prepared by a two-step annealing process in air. Zinc-based MOF (ZIF-8) and cobalt-based MOF (ZIF-67) were employed, respectively, as hard templates for the chemical encapsulation of $Ni(OH)_2$ nanostructures by hydrothermal synthesis. The as-prepared ZIF-8@$Ni(OH)_2$ and ZIF-67@$Ni(OH)_2$ were then converted to corresponding MMO through annealing in air. Meanwhile, MOF-derived carbon was preserved in the as-fabricated MMO structure, thus improving the electronic conductivity as well as the mechanical stability of the materials. In virtue of these features, high specific capacitance of 1017 and 744 $F{\cdot}g^{-1}$ can be delivered at a current density of 1 $A{\cdot}g^{-1}$ for the Co_3O_4@NiO and ZnO@NiO samples, respectively. In addition, both of the samples have shown excellent cycling performance, which exhibited excellent capacitance retentions of 90.1% and 93.0% after 10,000 cycles for the Co_3O_4@NiO and ZnO@NiO samples, respectively, demonstrating their very promising use in next-generation pseudocapacitors.

Metal–organic frameworks (MOF) have been extensively studied in the past two decades due to their designable frameworks formed by self-assembly reactions of metal ions and organic ligands [1–3]. Even though it is difficult to directly use the MOF materials for various applications because of their chemical instability, it provides the materials scientists with many possibilities to design and prepare MOF-derived porous materials with tunable structural and compositional features [4, 5]. Porous carbon, metal oxide, or other metal/carbon-based nanostructures can be obtained from MOF-based precursors by annealing in inert or air conditions, due to the coexistence of metallic, organic or other guest species in the frameworks [6–8]. For example, Tang et al. [9] reported the synthesis of N-doped carbon@graphitic carbon core–shell structure by direct pyrolysis of a precursor composed of ZIF-8 and ZIF-67. Hu et al. [10] demonstrated a double-shelled nanocages composed of $Co_3O4/NiCo_2O_4$, which are derived from ZIF-67/Ni-Co LDH. These MOF-derived nanostructures with various complexity might deliver multiple structure- and composition-dependent features, offering potential solutions to key challenges in important applications, such as lithium/sodium ion batteries, supercapacitors, photo/electrocatalysis, and biosensors [11, 12].

Pseudocapacitors have been considered as one of the promising types of supercapacitors in the past few years, which dominantly stores the energy by reversible Faradaic reactions occurring at the electrode surface [13]. Generally, these Faradaic reactions-based mechanisms can endow the pseudocapacitors much higher capacitance and energy density when compared to the carbon-based materials, because of the extra electrons stored in the form of chemical energy [14]. Thus, different types of metal oxide/sulfides, including MOF-derived metal oxides, were reported to enhance electrochemical property of the electrodes [15–19]. However, it is still a big challenge to balance high capacitance with good stability due to the highly porous character of the MOF-derived metal oxides that

Supplementary Information The online version contains supplementary material available at https://doi.org/10.1007/s12598-021-01836-8.

Y.-F. Ren, Z.-L. He, H.-Z. Zhao, T. Zhu*
School of Materials Science and Engineering, Central South University, Changsha 410083, China
e-mail: zhut0002@csu.edu.cn

may lead to severe volume change during the Faradaic reactions. For this reason, more attention should be paid to the thermal annealing process that are essential to the physical and chemical merits of the derived metal oxides [20]. In this work, as shown in Fig. 1, ZIF-8 and ZIF-67 precursors were coated with $Ni(OH)_2$ through a hydrothermal process, respectively. Then, a subsequent two-step annealing process was employed to prepare MOF-derived mixed metal oxides, namely ZnO@NiO and Co_3O_4@NiO. A relatively low temperature (200 °C) was used to pre-anneal the MOF precursors to preserve the structural and compositional features of the MOF intermediates. Then, a higher temperature (400 °C) was used to further anneal the MOF intermediates, leading to the formation of corresponding mixed metal oxides. Meanwhile, part of the carbon species was preserved in the structures, which can improve the electronic conductivity and alleviate the volume changes of the electrodes. In virtue of the high electroactivity and good electronic conductivity, the as-derived MMO exhibited a maximum capacitance of 1017 $F{\cdot}g^{-1}$ with a good cycling stability (90.1%) after 10,000 cycles. In addition, the carbon residue has played an important role for the balance of specific capacitance and cycle life.

The morphologies and compositions of all the materials were examined by scanning electron microscopy (SEM) and energy-dispersive spectrometer (EDS), and the results are displayed in Fig. 2. Both ZIF-8 and ZIF-67 particles show dodecahedral shapes with average particle sizes of 1 μm (Fig. 2a, e). After chemical growth of $Ni(OH)_2$, the surface of both ZIF-8 and ZIF-67 was encapsulated by nanosheets structures, which are typical layered double hydroxides (LDH), as shown in Fig. 2b, f. The nanosheets structures can be well preserved after thermal treatment, which can be reflected in Fig. 2c, g. In addition, the dodecahedral shapes can still be clearly observed after annealing, revealing the structural robustness of the particles.

The thermal treatments have converted the LDH to corresponding metal oxides, and part of the carbon species was retained due to this two-step annealing process. Further EDS results confirm the presence of C, O, Ni and Zn of ZnO@NiO sample (Fig. 2d), and the presence of C, O, Ni and Co of Co_3O_4@NiO sample (Fig. 2h), respectively. It is found that ZnO@NiO exhibits a higher carbon content (38.46%) than Co_3O_4@NiO (33.78%), which may result in different electronic conductivities of the samples. In addition, thermo-gravimetric analysis (TGA) was performed to study the decomposition behavior of the ZIF-8@$Ni(OH)_2$ precursor (Fig. S1a). It can be seen that there is a slight weight loss from 25 to 120 °C, which should be due to the evaporation of absorbed water. Then, a sharp weight drop starting around 250 °C can be observed, which can be assigned to the carbonization/combustion of organic species, and oxidation of $Ni(OH)_2$. The weight of the sample is gradually stabilized after 500 °C, indicating the completion of the thermal decomposition. TGA result of ZIF-67@$Ni(OH)_2$ is similar to that of ZIF-8@$Ni(OH)_2$. As shown in Fig. S1b, there are also two typical steps related to dehydration and carbonization/combustion, respectively. It can be found that the sharp weight drop of ZIF-67@$Ni(OH)_2$ started at around 320 °C, which indicates a different thermostability. Besides, the weight loss of ZIF-67@$Ni(OH)_2$ (58.8%) is much higher than that of ZIF-8@$Ni(OH)_2$ (34.0%), indicating a larger loss of organic species during the annealing process. This result can further explain the different C contents in ZnO@NiO and Co_3O_4@NiO. TGA behaviors have inspired us to use a two-step thermal treatment to convert the MOF precursors to MMO while preserving partial carbon residues of the samples. Besides, the two-step thermal treatment is essential for maintaining the dodecahedral morphology. As shown in Fig. S2, the nanostructures of ZIF-8@$Ni(OH)_2$ and ZIF-67@$Ni(OH)_2$ collapsed during a one-step annealing process because of the rapid phase transformation.

To examine the crystallography of the samples, X-ray diffraction (XRD) analysis was performed and compared. Figure 3a shows XRD patterns of ZIF-8 based precursor and respective derivatives. All the peaks can be assigned to ZIF-8, ZIF-8@$Ni(OH)_2$ (α-$Ni(OH)_2$, JCPDS No. 38-0715), and ZnO@NiO (hexagonal ZnO, JCPDS No. 89-0501; cubic NiO, JCPDS No. 89-7130) [21, 22], respectively. While for the ZIF-67 case (Fig. 3b), the derived MMO can be assigned to Co_3O_4 (JCPDS No. 76-1802) [23] and NiO (JCPDS No. 71-1179) [24]. The multiple components of

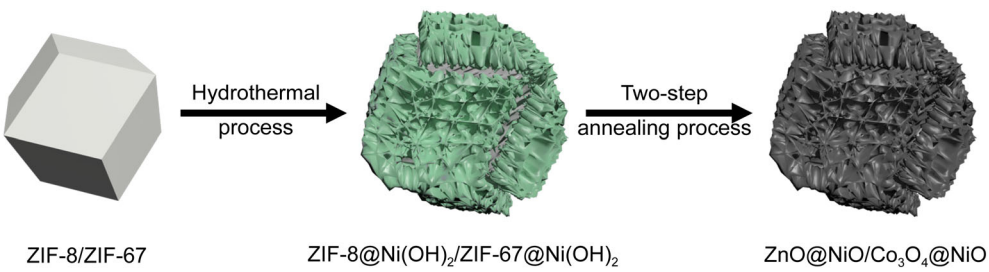

Fig. 1 Schematic illustration of synthesis process of ZnO@NiO and Co_3O_4@NiO

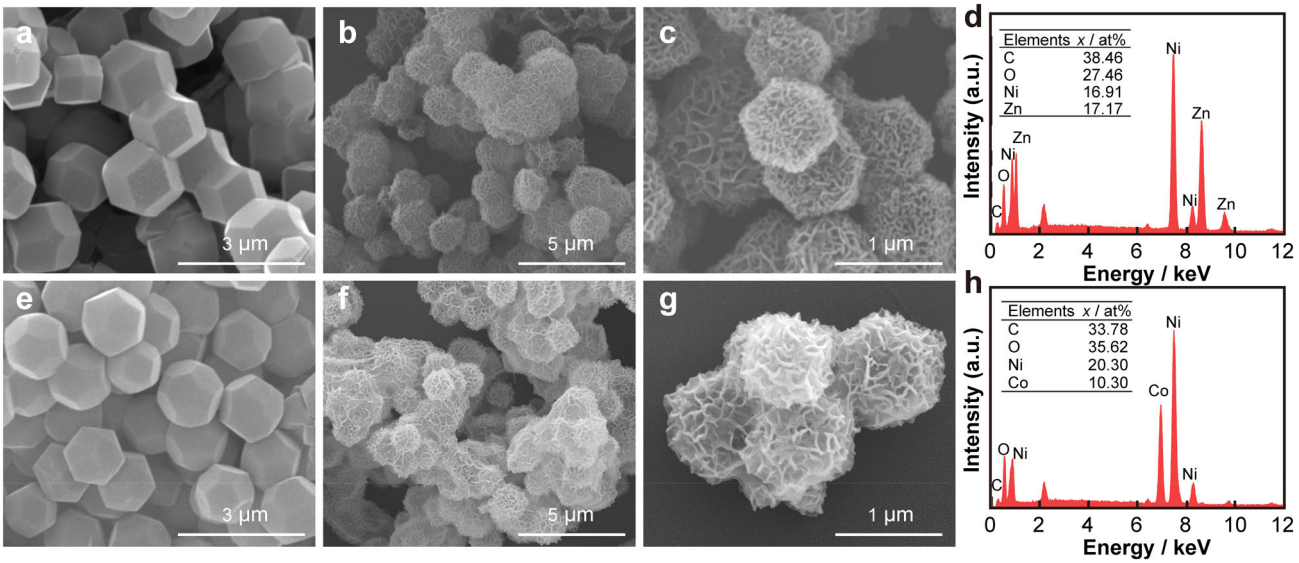

Fig. 2 SEM images of **a** ZIF-8, **b** ZIF-8@Ni(OH)$_2$, **c** ZnO@NiO, **e** ZIF-67, **f** ZIF-67@Ni(OH)$_2$ and **g** Co_3O_4@NiO; EDS patterns of **d** ZnO@NiO and **h** Co_3O_4@NiO

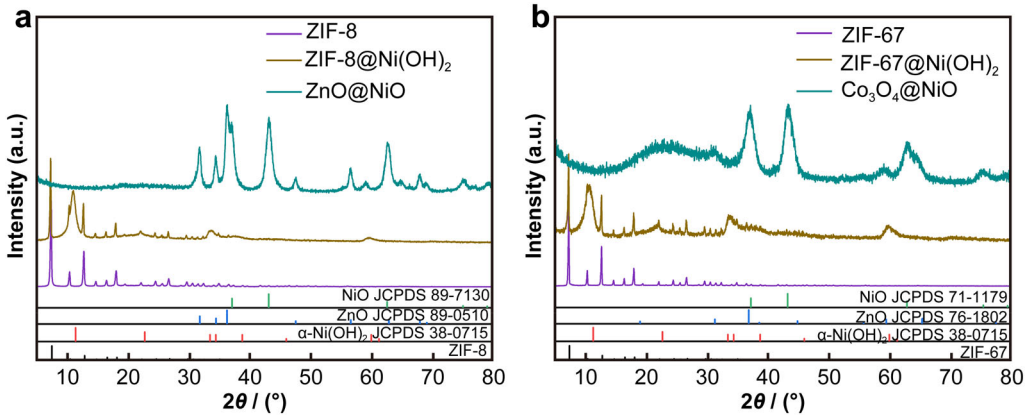

Fig. 3 XRD patterns of **a** ZIF-8 derived samples and **b** ZIF-67 derived samples

the MMO may endow the fabricated electrodes additional Faradaic reactions, thus remarkably enhancing the pseudocapacitance. We further conducted XPS tests to investigate the surface elemental composition and chemical state of the as-prepared ZnO@NiO and Co_3O_4@NiO, respectively. As shown in Fig. S3, Ni, Zn, O and C can be detected in ZnO@NiO. For Ni 2p (Fig. S3a), the two peaks at 853.8 eV ($2p_{3/2}$) and 871.5 eV ($2p_{1/2}$) together with two satellite peaks (identified as "Sat.") are ascribed to Ni^{2+}, while another two peaks at 855.5 eV ($2p_{3/2}$) and 873.3 eV ($2p_{1/2}$) are related to Ni^{3+} [25]. For Zn 2p (Fig. S3b), the two typical peaks at 1021.8 eV ($2p_{3/2}$) and 1044.8 eV ($2p_{1/2}$) reveal the existence of Zn^{2+} [26]. For O 1s (Fig. S3c), the peak at 529.1 eV (identified as "O1") indicates metal–oxygen bonds, while the peak at 531 eV (identified as "O2") is ascribed to the absorbed water or hydroxyl species [27]. For C 1s (Fig. S3d), the peaks related to sp^2 (284.5 eV), sp^3 (285.2 eV) and C=O (288.8 eV) can be observed, respectively [28]. It is worth noting that the sp^2 C can improve electronic conductivity of materials. X-ray photoelectron spectroscopy (XPS) results of Ni 2p (Fig. S4a), O 1s (Fig. S4c) in Co_3O_4@NiO are quite similar to that in ZnO@NiO, indicating the same reactions during hydrothermal and annealing processes. For Co 2p (Fig. S4b), the two peaks at 779.6 eV ($2p_{3/2}$) and 794.9 eV ($2p_{1/2}$) reveal the existence of Co^{3+}, while another two peaks at 781.4 eV ($2p_{3/2}$) and 796.5 eV ($2p_{1/2}$) are attributed to Co^{2+} [29, 30]. Although there are also three typical peaks related to sp^2, sp^3 and C=O (Fig. S4d), the ratio of sp^2/sp^3 is much smaller, indicating that the electronic conductivity of Co_3O_4@NiO is not as good as ZnO@NiO.

The CV measurements of the ZnO@NiO and Co_3O_4@NiO electrodes were carried out at different scan rates with the same potential window of 0–0.6 V (vs. SCE).

The CV curves shown in Fig. 4a, b clearly reveal paired redox peaks for both of the electrodes, which represent the pseudocapacitive characteristics of the materials [31]. Owing to the presence of inactive ZnO, the ZnO@NiO electrode delivers much lower current responses than those of Co_3O_4@NiO electrode at the same scan rate, because the latter contains the redox reactions from both Co and Ni species for energy storage. However, the ZnO@NiO electrode has preserved higher carbon content in the sample, which should be favorable to deliver good cycling stability. Subsequent GCD tests were conducted at various current densities with the same potential window of 0–0.55 V (vs. SCE), as shown in Fig. 4c, d. Both of the electrodes exhibit charge–discharge plateaus, which is consistent with the CV results. Also, the Co_3O_4@NiO electrode shows much longer charge–discharge time than ZnO@NiO, which should be due to the presence of electroactive Co_3O_4.

For a better comparison, CV curves at 2 $mV{\cdot}s^{-1}$ (Fig. 5a) and GCD curves at 1 $A{\cdot}g^{-1}$ (Fig. 5b) are separately displayed, which suggests higher capacitance of Co_3O_4@NiO than that of ZnO@NiO. It can be observed in Fig. 5a that ZnO@NiO has a wider full width half maximum (FWHM), while Co_3O_4@NiO has a lower redox peak potential. The wider FWHM can be ascribed to the higher C content of ZnO@NiO, which leads to a more obvious double-layer capacitance behavior. And the lower peak potential of Co_3O_4@NiO is mainly due to the integration of Co^{2+}/Co^{3+} redox peak, whose redox position is much lower than that of Ni^{2+}/Ni^{3+} [32]. The specific capacitance of the samples was then calculated based on the discharge curves obtained in Fig. 4c, d, and the results are presented in Fig. 5c. High specific capacitance of 744, 700, 606, 534, 318 $F{\cdot}g^{-1}$ can be delivered at current densities of 1.0, 2.5, 5.0, 10.0 and 25.0 $A{\cdot}g^{-1}$ for the ZnO@NiO electrode, respectively. Meanwhile, the Co_3O_4@NiO electrode exhibited higher capacitance of 1017, 850, 821, 740 and 568 $F{\cdot}g^{-1}$ at corresponding current densities. Moreover, the cycling stability tests were evaluated and compared at a very high current density of 25 $A{\cdot}g^{-1}$ (Fig. 5d). It can be seen that the Co_3O_4@NiO electrode exhibits much higher capacitance than ZnO@NiO. However, the latter has shown a better capacitance retention (93%) than the former (90.1%), which may be ascribed to the higher ratio of carbon residue and the robust ZnO core of ZnO@NiO. The carbon species may have played an important role in improving the electronic conductivity and alleviating the volume change of the electrodes during the charge and discharge process [33]. Besides, there should be no large

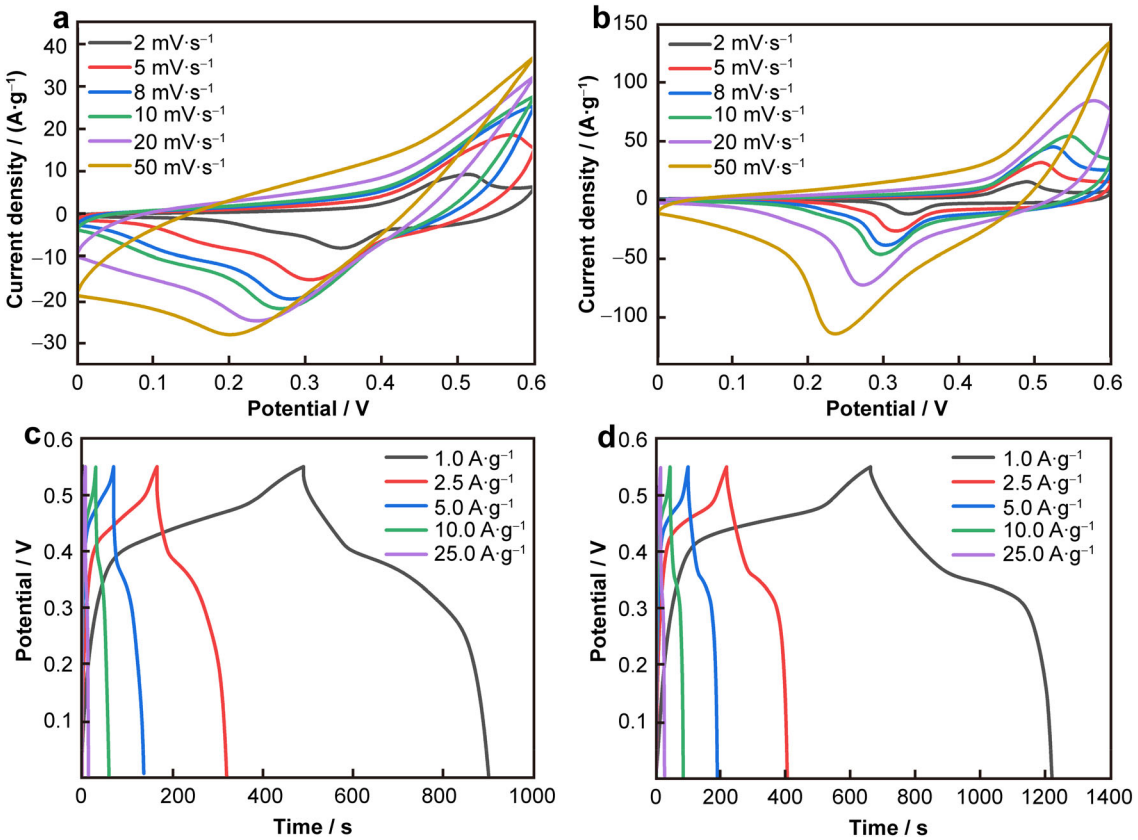

Fig. 4 CV curves obtained at various scan rates of **a** ZnO@NiO and **b** Co_3O_4@NiO; GCD curves obtained at various current densities of **c** ZnO@NiO and **d** Co_3O_4@NiO electrodes (all potentials are recorded versus SCE)

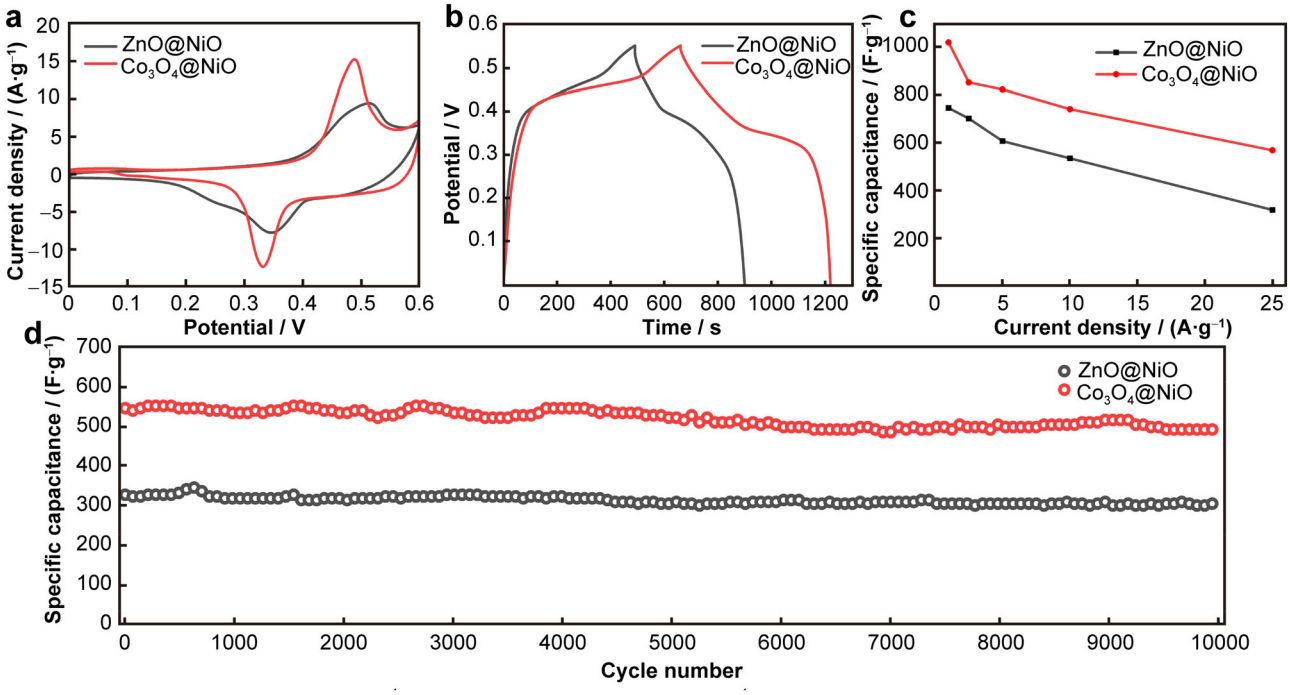

Fig. 5 **a** CV curves obtained at 2 $mV \cdot s^{-1}$, **b** GCD curves obtained at 1 $A \cdot g^{-1}$, **c** specific capacitance calculated from discharge curves at various current densities; **d** cycling performance at 25 $A \cdot g^{-1}$ of electrodes (all potentials are recorded versus SCE)

volume change of the inactive ZnO during cycling test, thus delivering a better structure stability of ZnO@NiO.

To further confirm the electronic conductivity of the electrodes, EIS measurements were performed and the results are displayed in Fig. S5. R_s represents the resistance of solution, including the electrolyte interface and ohmic resistance, R_{ct} is the transfer resistance and C_{dl} is the double-layer capacitance [34]. For the whole Nyquist plot, the X intercept indicates the R_s, while the radius of semicircle reveals the R_{ct}. The R_s value of ZnO@NiO is $\sim$ 3.6 Ω, which is smaller than that of Co_3O_4@NiO ($\sim$ 4 Ω), suggesting a better electronic conductivity of the former electrode. In the high-frequency region, the ZnO@NiO exhibits a semicircle, which shows an electrochemical behavior dominated by charge transfer. While Co_3O_4@NiO electrode shows a slightly larger radius of the semicircle, indicating its slower charge transfer. It should be noted that a larger slope of ZnO@NiO was observed than that of Co_3O_4@NiO in the low-frequency region, clearly verifying higher diffusion resistance of the former electrode. Therefore, the pseudocapacitive performance of the electrodes is consistent with the EIS analysis, which reflects the intrinsic property of charge transfer in the three-electrode system.

In summary, two types of MMO electrode materials, namely ZnO@NiO and Co_3O_4@NiO, were prepared by a two-step thermal treatment of MOF-based precursors. The as-prepared MMO electrodes have shown different ratios of carbon residues after thermal treatment due to different MOF precursors. When used as electrode materials for pseudocapacitors, Co_3O_4@NiO electrode exhibits a maximum capacitance of 1017 $F \cdot g^{-1}$ with a retention of 90.1% after 10,000 cycles. While ZnO@NiO electrode with higher carbon ratio delivered a lower specific capacitance of 744 $F \cdot g^{-1}$, but a better cycling stability (93.0%) after 10,000 cycles. Both of the electrodes have demonstrated very long cycling stability in pseudocapacitive materials, certifying their promising use in the next-generation pseudocapacitors.

Acknowledgements This work was financially supported by the Start-Up Grant of Central South University (No. 202045001), the Innovation-Driven Project of Central South University (No. 2019CX028) and Huxiang Assembly Program for High-level Talents (No. 2018RS3018).

Declarations

Conflict of interests The authors declare that they have no conflict of interest.

References

[1] Eddaoudi M, Kim J, Rosi N, Vodak D, Wachter J, O'Keeffe M, Yaghi OM. Systematic design of pore size and functionality in isoreticular MOFs and their application in methane storage. Science. 2002;295(5554):469.

[2] Zhang YB, Zhou HL, Lin RB, Zhang C, Lin JB, Zhang JP, Chen XM. Geometry analysis and systematic synthesis of highly porous isoreticular frameworks with a unique topology. Nat Commun. 2012;3:642.
[3] Guillerm V, Ragon F, Dan-Hardi M, Devic T, Vishnuvarthan M, Campo B, Vimont A, Clet G, Yang Q, Maurin G, Ferey G, Vittadini A, Gross S, Serre C. A series of isoreticular, highly stable, porous zirconium oxide based metal-organic frameworks. Angew Chemie-Int Ed. 2012;51(37):9267.
[4] Wu HB, Lou XW. Metal-organic frameworks and their derived materials for electrochemical energy storage and conversion: promises and challenges. Sci Adv. 2017;3(12):eaap9252.
[5] Zhu JY, Liang F, Yao YC, Ma WH, Yang B. Preparation and application of metal organic frameworks derivatives in electro-catalysis. Chin J Rare Met. 2019;43(2):186.
[6] Guan BY, Kushima A, Yu L, Li S, Li J, Lou XW. Coordination polymers derived general synthesis of multishelled mixed metal-oxide particles for hybrid supercapacitors. Adv Mater. 2017;29(17):1605902.
[7] Hu H, Zhang JT, Guan BY, Lou XW. Unusual formation of CoSe@carbon nanoboxes, which have an inhomogeneous shell, for efficient lithium storage. Angew Chemie-Int Ed. 2016;55(33):9514.
[8] Wu HB, Xia BY, Yu L, Yu XY, Lou XW. Porous molybdenum carbide nano-octahedrons synthesized via confined carburization in metal-organic frameworks for efficient hydrogen production. Nat Commun. 2015;6:6512.
[9] Tang J, Salunkhe RR, Liu J, Torad NL, Imura M, Furukawa S, Yamauchi Y. Thermal conversion of core-shell metal-organic frameworks: a new method for selectively functionalized nanoporous hybrid carbon. J Am Chem Soc. 2015;137(4):1572.
[10] Hu H, Guan BY, Xia BY, Lou XW. Designed formation of Co_3O_4/$NiCo_2O_4$ double-shelled nanocages with enhanced pseudocapacitive and electrocatalytic properties. J Am Chem Soc. 2015;137(16):5590.
[11] Guan BY, Yu XY, Wu HB, Lou XW. Complex nanostructures from materials based on metal-organic frameworks for electrochemical energy storage and conversion. Adv Mater. 2017;29(47):1703614.
[12] Wang Q, Shang L, Sun-Waterhouse D, Zhang T, Waterhouse G. Engineering local coordination environments and site densities for high-performance Fe-N-C oxygen reduction reaction electrocatalysis. SmartMat. 2021;2:154.
[13] Miller JR, Simon P. Materials science—electrochemical capacitors for energy management. Science. 2008;321(5889):651.
[14] Hu LB, Chen W, Xie X, Liu NA, Yang Y, Wu H, Yao Y, Pasta M, Alshareef HN, Cui Y. Symmetrical MnO_2-carbon nanotube-textile nanostructures for wearable pseudocapacitors with high mass loading. ACS Nano. 2011;5(11):8904.
[15] Liu JP, Jiang J, Cheng CW, Li HX, Zhang JX, Gong H, Fan HJ. Co_3O_4 nanowire@MnO_2 ultrathin nanosheet core/shell arrays: a new class of high-performance pseudocapacitive materials. Adv Mater. 2011;23(18):2076.
[16] Chen LF, Huang ZH, Liang HW, Guan QF, Yu SH. Bacterial-cellulose-derived carbon nanofiber@MnO_2 and nitrogen-doped carbon nanofiber electrode materials: an asymmetric supercapacitor with high energy and power density. Adv Mater. 2013;25(34):4746.
[17] Chun SE, Evanko B, Wang XF, Vonlanthen D, Ji XL, Stucky GD, Boettcher SW. Design of aqueous redox-enhanced electrochemical capacitors with high specific energies and slow self-discharge. Nat Commun. 2015;6:7818.
[18] Zuo WH, Li RZ, Zhou C, Li YY, Xia JL, Liu JP. Battery-supercapacitor hybrid devices: recent progress and future prospects. Adv Sci. 2017;4(7):1600539.
[19] Wang T, Chen HC, Yu F, Zhao XS, Wang HX. Boosting the cycling stability of transition metal compounds-based supercapacitors. Energy Storage Mater. 2019;16:545.
[20] Bretos I, Jimenez R, Ricote J, Calzada ML. Low-temperature crystallization of solution-derived metal oxide thin films assisted by chemical processes. Chem Soc Rev. 2018;47(2):291.
[21] Kumar S, Pandit V, Bhattacharyya K, Krishnan V. Sunlight driven photocatalytic reduction of 4-nitrophenol on Pt decorated ZnO-RGO nanoheterostructures. Mater Chem Phys. 2018;214:364.
[22] Li GF, Chuang PYA. Identifying the forefront of electrocatalytic oxygen evolution reaction: electronic double layer. Appl Catal B-Environ. 2018;239:425.
[23] He F, Liu KY, Zhong JJ, Zhang SR, Huang Q, Chen C. One dimensional nickel oxide-decorated cobalt oxide (Co_3O_4) composites for high-performance supercapacitors. J Electroanal Chem. 2015;749:89.
[24] Yang ZH, Xu FF, Zhang WX, Mei ZS, Pei B, Zhu X. Controllable preparation of multishelled NiO hollow nanospheres via layer-by-layer self-assembly for supercapacitor application. J Power Sources. 2014;246:24.
[25] Guo X, Yan K, Fan F, Zhang Y, Duan Y, Liu J. Controllable synthesis of a NiO hierarchical microspheres/nanofibers composites assembled on nickel foam for supercapacitor. Mater Lett. 2019;240:62.
[26] Huang C, Hao C, Ye Z, Zhou S, Wang X, Zhu L, Wu J. In situ growth of ZIF-8-derived ternary ZnO/$ZnCo_2O_4$/NiO for high performance asymmetric supercapacitors. Nanoscale. 2019;11(20):10114.
[27] He W, Liang Z, Ji K, Sun Q, Zhai T, Xu X. Hierarchical Ni-Co-S@Ni-W-O core–shell nanosheet arrays on nickel foam for high-performance asymmetric supercapacitors. Nano Res. 2018;11(3):1415.
[28] Chu M, Wang L, Li X, Hou M, Li N, Dong Y, Li X, Xie Z, Lin Y, Cai W, Zhang C. Carbon coated nickel-nickel oxide composites as a highly efficient catalyst for hydrogen evolution reaction in acid medium. Electrochim Acta. 2018;264:284.
[29] Cao F, Zhao M, Yu Y, Chen B, Huang Y, Yang J, Cao X, Lu Q, Zhang X, Zhang Z, Tan C, Zhang H. Synthesis of two-dimensional $CoS_{1.097}$/nitrogen-doped carbon nanocomposites using metal-organic framework nanosheets as precursors for supercapacitor application. J Am Chem Soc. 2016;138(22):6924.
[30] Ning WW, Chen LB, Wei WF, Chen YJ, Zhang XY. $NiCoO_2$/NiCoP@Ni nanowire arrays: tunable composition and unique structure design for high-performance winding asymmetric hybrid supercapacitors. Rare Met. 2020;39(9):1034.
[31] Zhou WW, Kong DZ, Jia XT, Ding CY, Cheng CW, Wen GW. $NiCo_2O_4$ nanosheet supported hierarchical core-shell arrays for high-performance supercapacitors. J Mater Chem A. 2014;2(18):6310.
[32] Guan C, Liu X, Ren W, Li X, Cheng C, Wang J. Rational design of metal-organic framework derived hollow $NiCo_2O_4$ arrays for flexible supercapacitor and electrocatalysis. Adv Energy Mater. 2017;7(12):1602391.
[33] Zhao XX, Feng JR, Liu JW, Lu J, Shi W, Yang GM, Wang GC, Feng PY, Cheng P. Metal-organic framework-derived ZnO/ZnS heteronanostructures for efficient visible-light-driven photocatalytic hydrogen production. Adv Sci. 2018;5(4):9.
[34] Hao ZB, He XC, Li HD, Trefilov D, Song YY, Li Y, Fu XX, Cui YS, Tang SC, Ge HX, Chen YF. Vertically aligned and ordered arrays of 2D MCo_2S_4@metal with ultrafast ion/electron transport for thickness-independent pseudocapacitive energy storage. ACS Nano. 2020;14(10):12719.